Dynamical Seasonal Prediction of the Southern African Summer Precipitation

Chaoxia Yuan[1], Tomoki Tozuka[2], Willem A. Landman[3]

and Toshio Yamagata[1]

[1]*Application Laboratory, JAMSTEC, Yokohama 236-0001, Japan*

[2]*Department of Earth and Planetary Science, Graduate School of Science,*

The University of Tokyo, Tokyo 113-0033, Japan

[3]*Council for Scientific and Industrial Research, Natural Resources and the Environment, and*

Department of Geography, Geoinformatics and Meteorology, University of Pretoria

1 *Pretoria, South Africa*

,

Corresponding author address: Dr. Chaoxia Yuan, Application Laboratory, JAMSTEC, Yokohama 236-0001. E-mail: chaoxia.yuan@jamstec.go.jp

Abstract

Prediction skills for southern African (16˚-33˚E, 22˚-35˚S) summer precipitation in the Scale Interaction Experiment-Frontier coupled model is assessed for the period of 1982-2008. Using three different observation datasets, deterministic forecasts are evaluated by anomaly correlation coefficients, whereas scores of relative operating characteristic and relative operating level are used to evaluate probabilistic forecasts. It is shown that these scores for forecasts of December-February precipitation initialized on October 1st are significant at 95% confidence level. On a local scale, the prediction skills in the northwestern and central parts of southern Africa are higher than those in northeastern South Africa. El Niño/Southern Oscillation (ENSO) provides the major source of predictability, but the relationship with ENSO is over-confident in the model. Also, the Benguela Niño, the basin mode in the tropical Indian Ocean, the subtropical dipole modes in the South Atlantic and the southern Indian Oceans and ENSO Modoki may provide additional sources of predictability. When prediction skills are evaluated for the whole wet season from October to the following April, it is found that precipitation anomalies in December-February are most predictable. The present study presents promising results for seasonal prediction of precipitation anomalies in the extratropics, where seasonal forecast are considered a difficult task.

1. Introduction

Precipitation over most of southern Africa shows a distinct seasonality with a wet season in austral summer and a dry season in austral winter. It undergoes significant interannual variations with El Niño/Southern Oscillation (ENSO) playing a key role (Dyer 1979; Lindesay 1988; Reason et al. 2000; Reason and Rouault 2002; Rouault and Richard 2005). In La Niña years, cloud bands related to the South Indian Convergence Zone tend to be preferentially located over southern Africa, resulting in higher precipitation. On the other hand, the cloud bands tend to move northeastward to Madagascar in El Niño years, leading to dry conditions in southern Africa (e.g., Cook 2000; Hart et al. 2010, 2012). However, the ENSO influences are neither simple nor exclusive. For example, the 1997/1998 El Niño, the strongest event on record, was not accompanied by the driest summer in subtropical southern Africa (Lyon and Mason 2007). Also, their link undergoes large decadal variations (Richard et al. 2000), and can be modified by local systems such as Angola low (Reason and Jagadheesha 2005; Lyon and Mason 2007).

Besides ENSO, large-scale atmospheric circulation anomalies associated with the subtropical dipole modes in the South Atlantic and the southern Indian Ocean (e.g., Venegas et al. 1997; Behera and Yamagata 2001) may modulate precipitation through their impacts on moisture transport (Behera and Yamagata 2001; Reason 2001, 2002; Vigaud et al. 2009). Also, recent studies showed that the subtropical dipole modes are closely related to the synoptic rain-bearing systems passing through southern Africa such as the tropical temperate troughs (Harrison 1984; Todd and Washington 1999; Fauchereau et al. 2009; Pohl et al. 2009;

Ratna et al. 2012; Vigaud et al. 2012). Furthermore, tropical cyclones (Reason and Keibel 2004), Angola low (Lyon and Mason 2007), Benguela upwelling system (Walker 1990) and Agulhas Current (Mason 1995; Tyson and Preston-Whyte 2004) exert influences on the southern African summer precipitation. Complex interactions among them make the seasonal prediction a difficult task.

Agriculture in southern Africa is predominantly rain-fed and thus highly vulnerable to rainfall variations, but measures to mitigate impacts of the interannual variations are still far below satisfaction (Conway 2009). To increase resilience of local communities and households, it is crucial to understand causes of rainfall variations, to make an accurate prediction, and to implement an early warning system and countermeasures. For this reason, the South African modeling community has developed operational seasonal forecasting systems (e.g., Barnston et al. 1996; Mason et al 1996; Landman and Mason 1999; Landman et al. 2001). The earlier systems relied on statistical methods and often adopted sea surface temperature (SST) in the adjacent subtropical oceans and/or the remote tropical eastern Pacific as predictors. More recently, they were replaced by two- and one-tiered dynamical forecast systems, but raw model outputs, such as geopotential height at 850 hPa, are often statistically downscaled to achieve better prediction skills of the southern African summer precipitation (e.g., Landman and Goddard 2002; Landman et al. 2012; Landman and Beraki 2012). This is because general circulation models tend to simulate large-scale circulation anomalies more accurately than precipitation anomalies (Landman and Goddard 2002). One of the reasons is that typical resolution of general circulation models (100-200 km) is too coarse to adequately resolve complex topography that is important to the local precipitation.

For this reason, some recent studies have developed dynamical downscaling systems for southern Africa using high-resolution regional models (Ratnam et al. 2011; Boulard et al. 2012; Crétat et al. 2012), but these models require good side boundary conditions provided by a global model.

In this regard, CGCMs have made big progresses in seasonal forecasts not only for the tropical climate variations (e.g., Luo et al. 2007; Jin et al. 2008; Barnston et al. 2012), but also for extratropical climate variations. Yuan et al. (2013) showed for the first time that the SST anomalies even in the subtropical oceans are predictable at around one season lead when they assessed predictability of the subtropical dipole modes. This presents a great potential for the CGCMs to predict the seasonal climate variations in the mid-latitudes, and encourages further development of CGCMs for mid-latitudes applications.

In this study, using the same CGCM as in Yuan et al. (2013), seasonal forecasts of the summer precipitation in southern Africa (16˚-33˚E and 22˚-35˚S, shown by the white box in Fig. 1a) are evaluated for the period of 1982-2008. A special emphasis is placed on precipitation anomalies in December-February (DJF), corresponding to the peak of the wet season in southern Africa. The model forecasts of the precipitation in DJF are verified against observations without any post-processing, and thus successful forecasts may be related to realistic reproductions of large-scale circulation anomalies responsible for observed precipitation anomalies. Therefore, by comparing the predicted and observed SST and large-scale circulation anomalies, possible sources of predictability may be investigated as well.

This paper is organized as follows. A brief description of the CGCM, retrospective

forecast experiments, and verification data and methods is given in the next section. In Section 3, the prediction skills for the precipitation anomalies in DJF when the model is initialized on October 1st are assessed. Possible sources of predictability are discussed in Section 4. Section 5 examines how prediction skills vary during the wet season. The final section is reserved for conclusions.

2. Model, retrospective forecasts, and verification data and methods

2.1. Model and retrospective forecasts

The Scale Interaction Experiment-Frontier Research Center for Global Change CGCM (SINTEX-F, see Luo et al. 2003 and 2005a for details) is used in this study. The oceanic component is the reference version 8.2 of Océan Parallélisé (Madec et al. 1998). It has 31 vertical levels and horizontal resolution of 2˚ with increased meridional resolution of 0.5˚ near the equator. The atmospheric component is the latest version of ECHAM4 (Roeckner et al. 1996) with 19 vertical levels and a horizontal resolution of T106. The coupled model has been used to successfully simulate and predict the tropical climate modes such as ENSO and the Indian Ocean Dipole and their teleconnections to the mid-high latitudes (e.g., Yamagata et al. 2004; Tozuka et al. 2005; Luo et al. 2005b, 2007, 2008). It has higher skills in simulating the Indian Ocean subtropical dipole mode than the Coupled Model Inter-comparison Project phase-3 (CMIP3) coupled models (Kataoka et al. 2012), and can skillfully predict the Indian Ocean and South Atlantic subtropical dipole modes with about one season lead (Yuan et al. 2013). In this study, a series of nine-member ensemble forecasts is conducted by the coupled model. The forecasts are initialized on the first day of each month from February 1982 to

December 2008 and integrated for 12 months. The nine ensemble members differ in initial conditions and/or coupling physics. Readers are referred to Luo et al. (2007) and Yuan et al. (2013) for more details.

2.2. Verification data and methods

The precipitation forecasts are verified against three different observations: Global Precipitation Climatology Project monthly precipitation (GPCP; 2.5˚x2.5˚; Adler et al. 2003), Global Precipitation Climatology Centre monthly precipitation (GPCC; 2.5˚x2.5˚; land only; Schneider et al. 2013) and Africa Rainfall Climatology version 2 daily precipitation estimates (ARC2; 0.1˚x0.1˚; Love et al. 2004). Although there are some missing data, an average of available dates in a month/season is used to calculate the monthly/seasonal mean of ARC2. The predicted SSTs and atmospheric fields are verified against the monthly Optimum Interpolation SST (OISST; 1˚x1˚; Reynolds et al. 2002) and three different reanalysis datasets, respectively. The latter includes the National Centers for Environmental Prediction/National Center for Atmospheric Research reanalysis 1 (NCEP/NCAR; 2.5˚x2.5˚; Kalnay et al. 1996), the European Centre for Medium-Range Weather Forecasts Interim Reanalysis (ERA-Interim; 1.5˚x1.5˚; Dee et al. 2011) and the NCEP climate forecast system reanalysis (CFSR; 2.5˚x2.5˚; Saha et al. 2010). We note that the data above have various horizontal resolutions and are interpolated to the model girds when needed.

Figure 1 shows the climatology of precipitation and moisture fluxes at 850 hPa in DJF. All three precipitation datasets show east-west gradient with the maximum in eastern South Africa separated from the inter-tropical convergence zone to the north. However, the

maximum precipitation is slightly larger in the GPCP than in the GPCC and ARC2 (Figs. 1a-c). The moisture fluxes to the southern African subcontinent are mainly from the Indian Ocean, and they are slightly stronger in the ERA-Interim than in the NCEP/NCAR and CFSR. Nevertheless, there are no significant differences in the three observed precipitation and reanalysis data. The model successfully simulates the observed precipitation pattern (Fig. 1d), but the simulated amount is about twice as large as the observed, because the simulated moisture fluxes to the subcontinent in the lower troposphere are much stronger and extend farther to the west compared to the reanalysis data. Similar wet biases have been reported in many general circulation and regional models (e.g., Joubert 1997; Ratnam et al. 2011; Crétat et al. 2012). To exclude the model biases in the climatology, predicted anomalies are verified against the observations after removing the monthly climatology in each dataset (Kirtman et al. 1997).

The southern African precipitation index in this study is defined as precipitation anomalies averaged over the southern African region of interest (16˚-33˚E, 22˚-35˚S; see the white box in Fig. 1a). Deterministic forecasts are evaluated by anomaly correlation coefficient (ACC; Pearson's correlation coefficient) between the ensemble-mean forecasts and observations. Its statistical significance is tested by the one-tailed *t*-test since the predicted and observed precipitation anomalies are supposed to correlate positively. Probabilistic forecasts for the above- and below-normal precipitation are evaluated by scores of the relative operating characteristic (ROC) and relative operating level (ROL) (Mason and Graham 1999). The threshold value for above (below)-normal tercile is the lowest (highest) value in the highest (lowest) 33% of the historical records. The ROC and ROL scores are equivalent to the

areas beneath the ROC and ROL curves. The ROC curve reflects the ratios between the hit rate and the false-alarm rate when the forecast probability to issue an above/below-normal precipitation year is decreased gradually. Here, the hit (false-alarm) rate is the proportion of years in the above/below-normal tercile (other terciles) that are correctly (incorrectly) predicted as the above/below-normal precipitation year. The ROL curve reflects the ratios between the correct-alarm ratio and the miss ratio when the number of years in the above/below-normal tercile is increased gradually, and the forecast for above/below-normal precipitation are issued when at least 33% of the ensemble members are in above/below-normal tercile. Here, the correct-alarm (miss) ratio is defined as the probability that an above/below-normal year will occur when it is forecasted (not forecasted). If the ROC and ROL scores are better than 0.5, the forecast system is regarded to have skills in discriminating the above/below-normal precipitation, and the higher the scores, the better the skills are. The statistical significance of the scores is tested by the Mann-Whitney U-test (Manson and Graham 2002). We note that all ROC and ROL scores shown in this study are cross-validated by a leave-one-out manner, such that the threshold is computed using all years except for the year being considered.

Since the ROC and ROL scores cannot reflect the reliability of the forecast probabilities, the reliability diagram is also provided (Wilks 1995). In the reliability diagram, the forecast probabilities are plotted against frequency by which the forecasts are verified (i.e. the observed relative frequency). Ideally, the reliability curve is along the 45˚ diagonal line, which signifies the identical forecast probability and observed relative frequency. If the curve lies above (below) the 45˚ diagonal line, the forecast system is under (over)-confident.

Besides being reliable, the forecast probabilities are desired to span away from the climatological probability, which is 33% in this study. The reason is that even without model predictions, the probability for the precipitations in each year to fall in the above/below-normal tercile is 33%.

3. Prediction skills for the DJF southern African precipitations

3.1. Deterministic forecasts

Figure 2 shows the time series of the southern African precipitation indices in DJF obtained from the model forecasts initialized on October 1st and the GPCP. Since the index based on GPCC (ARC2) is similar to that based on the GPCP with correlation coefficients of 0.99 (0.84), it is not shown in Fig. 2. The ensemble-mean forecasts have high correlations with the observation; when verified against the GPCP, GPCC and ARC2, the ACCs are 0.68, 0.66 and 0.61, respectively. These are significant at 99.95% confidence level by the one-tailed *t*-test and higher than 0.6, the threshold value of high prediction skills for seasonal precipitation (Marengo et al. 2005). We note that the observed precipitation index falls within the model's interquartile range in only seven out of 27 years, because the standard deviation of precipitation anomalies in each ensemble member is only two-third of the observation. Also, the large ensemble spread is due to one or two outliers.

The Spearman's (Kendall's tau rank) correlation coefficients are 0.71, 0.70 and 0.63 (0.55, 0.52 and 0.45), when the 27-year deterministic forecasts shown in Fig. 2 are verified against the GPCP, GPCC, and ARC2, respectively. All of these correlation coefficients are significant at 99.95% confidence level, and higher than those obtained in past studies. For

instance, using prediction results of three CGCMs from the Development of a European Multimodel Ensemble System for Seasonal-to-Interannual Prediction Project (DEMETER) initialized on November 1st, Landman and Beraki (2012) obtained statistically downscaled forecasts for DJF southern African precipitations averaged south of 10˚S. When their deterministic forecasts were verified against the University of East Anglia Climatic Research Unit (CRU; Mitchell and Jones 2005) monthly precipitation data for the 21-year test period from 1980/1981 to 2001/2002, the Spearman's rank correlation coefficient was slightly less than 0.5, significant at 95% confidence level. Also, for the 14-year test period from 1995/1996 to 2008/2009, the Kendall's tau rank correlation coefficient between the predicted rainfall in DJF obtained from statistical downscaling of a coupled model (ECHAM4.5-MOM3-DC2; DeWitt 2005) prediction initialized at the end of October and the rainfall data from the South African Weather Service (Van Rooy 1972) was 0.45, significant at 95% confidence level (Landman et al. 2012). Although there exist some differences in precipitation data used to evaluate the model, data period, area used to calculate average precipitation, and lead-time of seasonal forecasts, the high correlation coefficients obtained in this study suggest that the SINTEX-F has high skills in predicting the southern African summer precipitation.

Figure 3 shows the ACCs of predicted precipitation anomalies with the three different observations at each model grid in the southern African region of interest. Although the ACCs are somewhat higher with GPCP, their spatial distributions are quite similar; the ACCs significant at 95% confidence level are mostly confined to the northwestern and central part of southern Africa, while very low ACCs are found in northeastern South Africa. This is

contrasted to many other models showing the highest prediction skills in northeastern South Africa (e.g., Landman et al. 2012). Hence, a multi-model ensemble forecast system for the southern African summer precipitation may benefit from inclusion of the SINTEX-F, as it provides distinct and independent prediction skills (Hagedorn et al. 2005).

3.2. Probabilistic forecasts

The leave-one-out cross-validated ROC scores for the above (below)-normal DJF southern African precipitation indices in DJF are 0.76, 0.76 and 0.80 (0.79, 0.82 and 0.78), respectively, when the probabilistic forecasts are verified against the GPCP, GPCC and ARC2 (Fig. 4a). The corresponding ROL scores are 0.84, 0.84 and 0.80 (0.85, 0.85 and 0.80), respectively (Fig. 4b). These scores are statistically significant at 95% confidence level by the Mann-Whitney U-test. When the ROC and ROL scores are calculated at each model grid, the scores are higher than 0.5 in most summer rainfall regions of southern Africa except for northeastern South Africa (Figs. 5 and 6). Moreover, areas with the ROC and ROL scores above 0.7 are mostly confined to the northwestern and central parts of southern Africa. This is in accordance with the areas of the highest ACCs (Fig. 3), suggesting the consistency among the different verification methods.

Figure 7 shows the reliability curves and frequency histograms of the forecast probabilities for the above- and below-normal precipitation. The regression lines weighted by the frequency of forecast probabilities for the reliability curves are also superimposed. We note that the 27-year probabilistic forecasts for precipitation anomalies at each of 221 model grids in the southern African region of interest are included for the reliability examination,

and the sample size is thus increased to 5967. It is shown that the reliability curves for both the above- and below-normal precipitation are below (above) the diagonal line at the high (low) end of the forecast probabilities, indicating that the above- and below-normal precipitation occur less (more) frequently than predicted. Moreover, the forecast probabilities do not span much away from 33%, the climatological probability. These are common problems suffered by many CGCMs in predicting the southern African summer precipitation and need to be addressed in the future (e.g., Landman and Beraki 2012; Landman et al. 2012).

4. Large-scale circulation anomalies related to the above/below-normal precipitations and possible sources of predictability

In light of the good skill in predicting the southern African precipitation anomalies in DJF, we use the present model to investigate the relevant large-scale circulation anomalies and possible sources of predictability. As indicated in Fig. 2, the model successfully predicts five (six) of the total nine years in the above (below)-normal precipitation tercile. Those five (six) years are 1988/1989, 1995/1996, 1999/2000, 2005/2006 and 2007/2008 (1982/1983, 1986/1987, 1991/1992, 1994/1995, 2000/2001 and 2006/2007). We have constructed DJF composites for the successfully predicted years, and discuss possible reasons why the prediction fails in the remaining years. Since qualitatively the same results are obtained even if we use the GPCC and ARC2, we only present results from the GPCP in this section.

Positive (negative) precipitation anomalies are observed in vast areas of southern Africa south (north) of 15˚S in the successfully predicted above-normal precipitation years (Fig. 8a). This indicates a southward shift of the inter-tropical convergence zone and it may be

associated with weakening and a southward shift of the South Atlantic and Indian Ocean subtropical highs (Figs. 9a, c, e; Cook et al. 2004; Vigaud et al. 2009). Negative geopotential height anomalies in the lower troposphere cover almost the whole southern African subcontinent. The anomalous center in the southeastern Atlantic Ocean off the coast of Namibia is related to anomalous moist westerlies and northwesterlies from the South Atlantic Ocean to the subcontinent. In addition, the anomalous southeast-northwest pressure gradient over southern Africa is conducive to anomalous moist northeasterlies and easterlies from the western Indian Ocean to the subcontinent. As a result, the humidity in the lower troposphere is increased significantly (Figs. 10a-c) and convections are enhanced (Figs. 11a-c), resulting in more precipitation over southern Africa (Fig. 8a). Anomalies in the successfully predicted below-normal years are close to a mirror image of the above (Figs. 8c, 9b, d, f, 10e-g, 11e-g). Note that the anomalous patterns of atmospheric fields derived from the three reanalysis data are qualitatively consistent, but show some differences on a local scale, especially in the specific humidity and outgoing longwave radiation anomalies (Figs. 10-11). However, these differences do not influence our conclusions.

The model predicts to some extent the weakening and southward shift of the South Atlantic and Indian Ocean subtropical highs (Fig. 9g), the negative geopotential height anomalies in the lower troposphere over southern Africa, and the anomalous center in the southeastern Atlantic Ocean off Namibia. As a result, the anomalous northwesterlies and westerlies from the South Atlantic Ocean to southern Africa, the increased specific humidity in the lower troposphere (Fig. 10d), the enhanced convection (Fig. 11d), and positive precipitation anomalies are also predicted reasonably well in the above-normal years (Fig. 8b).

However, the predicted cyclonic circulation anomalies in the southeastern Atlantic Ocean are much weaker than the observed, and thus less moisture is fed from the South Atlantic to the subcontinent. Also, the strong cyclonic circulation anomalies centered at around 35˚E and 20˚S (Fig. 9g) are prohibiting the anomalous moist westerlies and northwesterlies from the Atlantic Ocean to extend eastward to the eastern part of southern Africa. This may lead to less feeding of moisture to northeastern South Africa (Fig. 10d), less active convection (Fig. 11d) and precipitation biases there (Figs. 8a-b). The forecasted precipitation and atmospheric circulation anomalies in the successfully predicted below-normal years are almost a mirror image of those in the successfully predicted above-normal years (Figs. 8d, 9h, 10h, 11h).

The circulation anomalies in the lower troposphere over southern Africa seen in the successfully predicted above/below-normal precipitation years (Fig. 9) remind us of the ENSO influence (e.g., Tyson and Preston-Whyte 2004). In fact, among the five successfully predicted above-normal years, all have a distinct La Niña signal in the tropical Pacific, and among six successfully predicted below-normal years, all but the 2000/2001 austral summer have a distinct El Niño signal. As a result, composites of SST anomalies in these successfully predicted years exhibit significant ENSO signals (Figs. 12a, c), and those of atmospheric circulation anomalies (Fig. 9) are dominated by the ENSO-related teleconnections (Fig. 13). It is not surprising that ENSO provides the dominant source of predictability. Landman and Beraki (2012) also showed that their multi-model ensemble forecast system has better prediction skills of southern African summer precipitation in the ENSO years than neutral years. This is not only because of the close relation between ENSO and the southern African summer precipitation, but also because ENSO itself is a highly predictable climate mode

providing dominant sources of predictability for the global climate variations. Hence, the high prediction skills of the southern African summer precipitation in the SINTEX-F may be due to its high skills predicting ENSO (Jin et al. 2008) and the associated large-scale teleconnections in the Southern Hemisphere (Figs. 9g-h, 13g-h; Yuan et al. 2013). A separate 100-year control experiment confirms the robustness of the above relationship in the SINTEX-F; the above (below)-normal precipitation in southern Africa is associated with La Niña (El Niño) (figure not shown).

However, the model is over-confident in simulating the link between ENSO and southern African summer precipitation. The correlation coefficient between the predicted Niño-3 and southern African precipitation indices in DJF is -0.77, which is higher than -0.57 in the observation. This may explain why 1997/1998 is predicted as the driest summer in association with the strongest 1997/1998 El Niño event even though it was not accompanied by the driest summer in subtropical southern Africa (Lyon and Mason 2007).

Also, the model shows some biases in simulating the relationship on a local scale. As shown in Figs. 14a and d, the observed precipitation anomalies over northeastern South Africa in DJF are negatively correlated with ENSO, but they are positively correlated in the model. This is probably because of model biases in circulation anomalies in the lower troposphere associated with La Niña (El Niño); cyclonic (anticyclonic) circulation anomalies in the southeastern Atlantic Ocean are too weak and cyclonic (anticyclonic) circulation anomalies over southern Africa centered at around 35˚E and 20˚S are too strong in the model (Fig. 13). We have discussed above that this may cause the precipitation biases in northeastern South Africa and result in the lower prediction skills there (Figs. 3, 5-6).

There may be other sources of predictability beside ENSO, because significant SST anomalies are found outside of the tropical eastern Pacific (Fig. 12). The SST anomalies along the coast of Angola and Namibia are associated with Benguela Niño, which is closely related to precipitation anomalies in the western part of southern Africa (Rouault et al. 2003; Florenchie et al. 2003). Since it is predicted relatively well in the 1990s, it may partly explain the better prediction skills in this decade when the correlation between ENSO and the southern African summer precipitation is relatively weak (Fig. 15).

Also, the basin-wide cooling (warming) in the tropical Indian Ocean in the above (below)-normal precipitation years (Fig. 12) may modulate the moisture fluxes from the Indian Ocean to southern Africa and contribute to positive (negative) precipitation anomalies (Goddard and Graham 1999). Although these SST anomalies are induced by ENSO through an atmospheric bridge (e.g., Klein et al. 1999; Xie et al. 2009), they are essential to simulate the correct precipitation response to ENSO in southern Africa (Goddard and Graham 1999).

In addition, Fig. 12 shows SST anomalies in the South Atlantic and the southern Indian Ocean associated with the subtropical dipole modes. It is not clear to which extent the subtropical dipole modes can provide an additional independent source of predictability for the summer precipitation, since the subtropical dipole modes are related to ENSO (e.g., Hermes and Reason 2005; Yuan et al. 2013; Morioka et al. 2013). The correlation coefficient between the Niño-3 and South Atlantic (Indian Ocean) subtropical dipole indices in DJF is -0.59 (-0.35) for the observation and -0.55 (-0.36) for the model. These correlations are significant at 95% confidence level. Here, the subtropical dipole mode indices are defined as the difference in SST anomalies between the southwestern and northeastern poles as in Yuan

et al. (2013). Therefore, the correlation coefficients between the subtropical dipole modes and precipitation anomalies are similar to those between the ENSO and precipitation anomalies with opposite signs in both the observation (Figs. 14a-c) and the model (Figs. 14d-f). Nevertheless, successful predictions of the subtropical dipole modes are important, because some impacts of ENSO on the southern African summer precipitation may be through the subtropical dipole modes via changing intensity and frequency of the synoptic rain-bearing systems (Pohl et al. 2009; Vigaud et al. 2012).

The coupled model successfully predicts the La Niña Modoki in the tropical Pacific and the below-normal precipitations in southern Africa in the austral summer of 2000/2001. According to Ratnam et al. (2013a), La Niña Modoki is associated with the negative, though not statistically significant, precipitation anomalies in South Africa. Hence, if the ENSO Modoki is successfully predicted, it may provide an additional source of predictability for the southern African summer precipitation.

There are three below-normal precipitation years that the model fails to predict (1983/1984, 1989/1990 and 2002/2003). Although these years are not dry enough to become the nine driest years (Fig. 2), they are predicted as the 12^{th}, 13^{th} and 11^{th} driest years, respectively. Among the four above-normal precipitation years that the model fails to predict (1987/1988, 1990/1991, 1993/1994 and 2008/2009), 1993/1994 and 2008/2009 are predicted as the 10^{th} and 12^{th} wettest years. In the austral summer of 1987/1988, the observed El Niño decayed quickly in the tropical Pacific, but the predicted El Niño lasts much longer, resulting in the dominant El Niño-related circulation anomalies over southern Africa and the 10^{th} driest summer in the model. Although 1990/1991 was an El Niño Modoki year, the model predicts

for a canonical El Niño year and thus negative precipitation anomalies over southern Africa.

5. Discussions

To check whether prediction skills vary during the wet season of southern Africa generally spanning from October to the following April, we have calculated ACCs of three-month precipitation anomalies at various lead times (Fig. 16). By no surprise, precipitation anomalies in DJF are most predictable (Figs. 16i-l). This is expected because the atmospheric circulation over southern Africa is predominantly influenced by the tropics in DJF, and thus the potential predictability of precipitation is highest (e.g., Landman and Mason 1999; Landman et al. 2009). The figure also suggests that predictions initialized on October 1st have much better skills than those initialized on September 1st (Figs. 10k-l). Besides the shorter lead-time, the initial information at the beginning of October may be important for a coupled model to predict the onset of the wet season; it usually starts in October, but it is difficult to simulate by general circulation models (Tozuka et al. 2013). On the other hand, the prediction skills are not much different with initialization dates of October, November and December 1st (Figs. 10i-k). This may be because ENSO, which provides the major source of predictability, is consistently well predicted. The ACCs of Niño-3 index in DJF are almost the same with 0.95 (±0.02) for predictions initialized on October, November and December 1st.

On regional scale, the highest ACCs are confined to the western and central parts of southern Africa, while low ACCs are found in northeastern South Africa. The low prediction skills in the latter may be partly due to the model biases in the ENSO-related teleconnections. In addition, they may be partly attributable to the coarse model resolution. The precipitation

in northeastern South Africa is strongly influenced by the escarpment (Garstang et al. 1987), but the SINTEX-F is too coarse to realistically represent this complex topography. For this reason, Ratnam et al. (2013b) recently used a regional model with horizontal resolution of 30 km to dynamically downscale prediction results from the SINTEX-F, and achieved better prediction skills in northeastern South Africa.

6. Conclusions

We have assessed skills of the SINTEX-F coupled model in predicting the summer precipitation in southern Africa (16˚-33˚E and 22˚S-35˚S) for the period of 1982-2008, and discussed possible sources of predictability. The ACCs of southern African precipitation indices in DJF are 0.68, 0.67 and 0.61, respectively, when the deterministic forecasts initialized on October 1st are verified against GPCP, GPCC and ARC2. These are significant at 99.95% confidence level by the one-tailed *t*-test, and higher than the 0.6 threshold value of high prediction skills for seasonal precipitation (Marengo et al. 2005). The leave-one-out cross-validated ROC scores for the probabilistic forecasts of the above (below)-normal precipitation are 0.76, 0.76 and 0.80 (0.79, 0.82 and 0.78), respectively, when verified against GPCP, GPCC and ARC2. The corresponding ROL scores are 0.84, 0.84 and 0.80 (0.85, 0.85 and 0.80), respectively. These scores are significant at 95% confidence level by the Mann-Whitney U-test.

On a local scale, the model has the highest prediction skills in the western and central parts of southern Africa, while skills are lower in northeastern South Africa. The lower prediction skills in the latter region may be related to the model biases in the ENSO-related

teleconnections in the southern African region. Also, the coarse model resolution may contribute to the lower skills, because the model cannot resolve the complex topography in northeastern South Africa that is crucial for the deep convection in austral summer (Garstang et al. 1987).

When prediction skills are evaluated for the whole wet season of southern Africa from October to the following April, we have found that precipitation anomalies in DJF are most predictable. This is consistent with the prevalent view that the atmospheric circulation over southern Africa in DJF is predominantly influenced by the tropics, and thus the potential predictability is highest.

It is shown that ENSO provides the dominant source of predictability. Among the five above-normal precipitation years that are successfully predicted by the model initialized on October 1st, all have distinct La Niña signals in the tropical Pacific, and among the six successfully predicted below-normal years, five have distinct El Niño signals. Hence, the high skills of the SINTEX-F model in predicting the southern African summer precipitation may be due to the high predictability of ENSO (Luo et al. 2008; Jin et al. 2008) and the robust ENSO-southern African summer precipitation relationship. However, the model is over-confident in simulating the relationship.

Besides ENSO, the Benguela Niño may contribute to better prediction sills, especially in the 1990s. The basin-wide SST anomalies in the tropical Indian Ocean and the subtropical dipole modes in the South Atlantic and the southern Indian Ocean may provide additional sources of predictability, although they are not totally independent of ENSO (Fig. 14; Hermes and Reason 2005; Yuan et al. 2013; Morioka et al. 2013). Also, we cannot exclude other

sources of predictability such as the ENSO Modoki in the tropical Pacific; the model successfully predicts the below-normal precipitation in southern Africa in the austral summer of 2000/2001 probably due to a successful prediction of La Niña Modoki and its teleconnection (Ratnam et al. 2013a).

The present study has provided promising results for seasonal prediction of precipitation anomalies in the extratropics, where seasonal forecasts are considered difficult. This encourages us to further downscale the model outputs by using a regional model (Ratnam et al. 2013b) so that seasonal forecast information may be more readily used. A real-time dynamical downscaling seasonal forecast for the southern African precipitation is carried out in our group for the societal applications.

Acknowledgments

Constructive comments provided by two anonymous reviewers helped us to improve the earlier manuscript. The SINTEX-F model was run on the Earth Simulator of Japan Agency for Marine-Earth Science and Technology. The ARC2 data is downloaded from the data library of the International Research Institute for Climate and Society. The present research is supported by the Japan Science and Technology Agency (JST) and Japan International Cooperation Agency (JICA) through Science and Technology Research Partnership for Sustainable Development (SATREPS).

References

Adler, RF, Huffman GJ, Chang A, Ferraro R, Xie P, Janowiak J, Rudolf B, Schneider U, Curtis S, Bolvin D, Gruber A, Susskind J, and Arkin P (2003) The Version 2 Global Precipitation Climatology Project (GPCP) monthly precipitation analysis (1979-Present). J Hydrometeor 4:1147-1167

Barnston AG, Thiao W, Kumar V (1996) Long-lead forecasts of seasonal precipitation in Africa using CCA. Weather Forecast 11:506-520

Barnston AG, Tippett MK, L'Heureux ML, Li S, DeWitt DG (2012) Skill of real-time seasonal ENSO model predictions during 2002-11. Bull Amer Meteor Soc 93:631-651

Behera SK, Yamagata T (2001) Subtropical SST dipole events in the southern Indian Ocean. Geophys Res Lett 28:327–330

Boulard D, Pohl B, Crétat J, Vigaud N, Pham-Xuan T (2013) Downscaling large-scale climate variability using a regional climate model: The case of ENSO over southern Africa. Clim Dyn 40:1141-1168

Crétat J, Pohl B, Richard Y, Drobinski P (2012) Uncertainties in simulating regional climate of southern Africa: Sensitivity to physical parameterizations using WRF. Clim Dyn 38:613-634

Conway G (2009) The science of climate change in Africa: Impacts and adaptation. Discussion Paper No. 1, Grantham Institute for Climate Change, Imperial College London, London, United Kingdom

Cook KH (2000) The South Indian Convergence Zone and interannual rainfall variability over southern Africa. J Clim 13:3789-3804

Cook C, Reason CJC, Hewitson BC (2004) Wet and dry spells within particularly wet and dry summers in the South African summer rainfall region. Clim Res 26:17-31

Dee DP and Coauthors (2011) The ERA-Interim reanalysis: Configuration and performance of the data assimilation system. Q J R Meteorol Soc 137:553-597

Dyer TGJ (1979) Rainfall along the east coast of Southern Africa, the southern oscillation and the latitude of the subtropical high pressure belt. Q J R Meteorol Soc 105:445-451

Fauchereau N, Pohl B, Reason CJC, Rouault M, Richard Y (2009) Recurrent daily OLR patterns in the southern Africa/southwest Indian Ocean region, implication for South African rainfall and teleconnections. Clim Dyn 32:575–591

Florenchie P, Lutjeharms JRE and Reason CJC (2003) The source of Benguela Niño in the South Atlanic Ocean. Geophys Res Lett 30. doi:10.1029/2003GL017172

Garstang M, Kelbe BE, Emmitt GD, London WB (1987) Generation of convective storms over the escarpment of northeastern South Africa. Mon Weather Rev 115:429-443

Goddard L and Graham NE (1999) Importance of the Indian Ocean for simulating rainfall anomalies over eastern and southern Africa. J Geophys Res 104:19099-19116

Hagedorn R, Doblas-Reyes FJ, Palmer TN (2005) The rationale behind the success of multi-model ensembles in seasonal forecasting – I. Basic concept. Tellus 57A:219-233

Harrison MSJ (1984) A generalized classification of South African summer rain-bearing synoptic systems. J Climatol 4:547-560

Hart NCG, Reason CJC, Fauchereau N (2010) Tropical-extratropical interactions over southern Africa: Three cases of heavy summer season rainfall. Mon Weather Rev 138:2608-2623

Hart NCG, Reason CJC, Fauchereau N (2012) Building a tropical-extratropical cloud band metbot. Mon Weather Rev 140:4005-4016

Hermes JC and Reason CJC (2005) Ocean model diagnosis of interannual coevolving SST variability in the South Indian and South Atlantic Oceans. J Clim 18:2864-2882

Jin EK, Kinter L III, Wang B, Kang IS, Shukla J, Kirtman BP, Kug JS, Yamagata T, Luo JJ, Schemm J, Kumar A (2008) Current status of ENSO prediction skill in coupled ocean-atmosphere models. Clim Dyn 31: 647-664

Joubert AM (1997) Simulations by the atmospheric model intercomparison project of atmospheric circulation over southern Africa. Int J Climatol 17:1129-1154

Kalnay E and Coauthors (1996) The NCEP/NCAR 40-year reanalysis project. Bull Amer Meteor Soc 77:437–471

Kataoka T, Tozuka T, Masumoto Y, Yamagata T (2012) The Indian Ocean subtropical dipole mode simulated in the CMIP3 models. Clim Dyn 39:1385-1399

Kirtman BP, Shukla J, Huang B, Zhu Z, Schneider EK (1997) Multiseasonal predictions with a coupled tropical ocean-global atmosphere system. Mon Weather Rev 125:789-808

Klein SA, Soden BJ, Lau NC (1999) Remote sea surface temperature variations during ENSO: Evidence for a tropical atmospheric bridge. J Clim 12:917-932

Landman WA, Beraki A (2012) Multi-model forecast skill for mid-summer rainfall over southern Africa. Int J Climatol 32:303-314

Landman WA, DeWitt D, Lee DE, Beraki A, Lötter D (2012) Seasonal rainfall prediction

skill over South Africa: One- versus two-tiered forecasting systems. Weather Forecast 27:489-501

Landman WA, Goddard L (2002) Statistical recalibration of GCM forecasts over southern Africa using model output statistics. J Clim 15:2038-2055

Landman WA, Mason SJ (1999) Operational long-lead prediction of South African rainfall using canonical correlation analysis. Int J Climatol 19:1073-1090

Landman WA, Mason SJ, Tyson PD, Tennant WJ (2001) Retroactive skill of multi-tiered forecasts of summer rainfall over southern Africa. Int J Climatol 21:1-19

Lindesay JA (1988) South African rainfall, the Southern Oscillation, and a Southern Hemisphere semi-annual cycle. J Clim 8:17-30

Love TB, Kumar V, Xie P, Thiaw W (2004) A 20-year daily Africa precipitation climatology using satellite and gauge data. Proceeding of the 84th AMS annual meeting, Seattle, Washington.

Luo JJ, Masson S, Behera SK, Gualdi S, Navarra A, Yamagata T (2003) South Pacific origin of the decadal ENSO-like variation as simulated by a coupled GCM. Geophys Res Lett 30. doi:10.1029/2003GL018649

Luo JJ, Masson S, Roeckner E, Madec G, Yamagata T (2005a) Reducing climatology bias in an ocean-atmosphere CGCM with improved coupling physics. J Clim 18:2344–2360

Luo JJ, Masson S, Behera SK, Shingu S, Yamagata T (2005b) Seasonal climate predictability in a coupled AOGCM using a different approach for ensemble forecast. J Clim 18:4474-4497

Luo JJ, Masson S, Behera SK, Yamagata T (2007) Experimental forecasts of the Indian

Ocean Dipole using a coupled OAGCM. J Clim 20:2178–2190

Luo JJ, Masson S, Behera SK, Yamagata T (2008) Extended ENSO predictions using a fully coupled ocean-atmosphere model. J Clim 21:84–93

Lyon B, Mason SJ (2007) The 1997-98 summer rainfall season in southern Africa. Part I: Observations. J Clim 20:5134-5148

Madec G, Delecluse P, Imbard M, Levy C (1998) OPA 8.1 ocean general circulation model reference manual. Tech. Rep. Note 11, LODYC/IPSL, Paris, France

Marengo J, Alves LM, Camargo H (2005) Global climate predictability at seasonal to interannual time scales. GEWEX News, Vol. 15, No.4, International GEWEX Project Office, Sliver Spring, MD, 6-7

Mason SJ (1995) Sea-surface temperature-South African rainfall associations, 1910-1989. Int J Climatol 15:119–135

Mason SJ, Graham NE (1999) Conditional probabilities, relative operating characteristics, and relative operating levels. Weather Forecast 14:713-725

Mason SJ, Graham NE (2002) Areas beneath the relative operating characteristics (ROC) and relative operating levels (ROL) curves: Statistical significance and interpretation. Q J R Meteorol Soc 128:2145-2166

Mason SJ, Joubert AM, Cosijn C, Crimp SJ (1996) Review of seasonal forecasting techniques and their applicability of southern Africa. Water SA 22:203-209

Morioka Y, Tozuka T, Yamagata T (2010) Climate variability in the southern Indian Ocean as revealed by self-organizing maps. Clim Dyn 35:1059–1072

Morioka Y, Tozuka T, Yamagata T (2011) On the growth and decay of the subtropical dipole

mode in the South Atlantic. J Clim 24:5538－5554

Morioka Y, Tozuka T, Yamagata T (2013) How is the Indian Ocean subtropical dipole excited? Clim Dyn. doi: 10.1007/s00382-012-1584-9

Pohl B, Fauchereau N, Richard Y, Rouault M, Reason CJC (2009) Interactions between synoptic, intraseasonal and interannual convective variability over southern Africa. Clim Dyn 33:1033-1050

Ratna SB, Behera SK, Ratnam JV, Takahashi K, Yamagata T (2012) An index for tropical temperate troughs over southern Africa. Clim Dyn. doi:10.1007/s00382-012-1540-8

Ratnam JV, Behera SK, Masumoto Y, Takahashi K, Yamagata T (2012) A simple regional coupled model experiment for summer-time climate simulation over southern Africa. Clim Dyn 39:2207-2217

Ratnam JV, Behera SK, Masumoto Y, Yamagata T (2013a) Tropical Pacific influences on the austral summer precipitation of southern Africa. Clim Dyn (in revision)

Ratnam JV, Behera SK, Ratna SB, Rautenbach CJ, Lennard C, Luo JJ, Masumoto Y, Takahashi K, Yamagata T (2013b) Dynamical downscaling of austral summer climate forecasts over southern Africa using a regional coupled model. J Clim (submitted)

Reason CJC (2001) Subtropical Indian Ocean dipole events and southern African rainfall. Geophys Res Lett 28:2225–2227

Reason CJC (2002) Sensitivity of the southern African circulation to dipole sea-surface temperature patterns in the South Indian Ocean. Int J Climatol 22:377-393

Reason CJC, Allan RJ, Lindesay JA, Ansell TJ (2000) ENSO and climatic signals across the Indian Ocean basin in the global context: Part 1, interannual composite patterns. Int J

Climatol 20:1285-1327

Reason CJC, Jagadheesha D (2005) Relationships between South Atlantic SST variability and atmospheric circulation over the South African region during austral winter. J Clim 18:3339-3355

Reason CJC, Keibel A (2004) Tropical cyclone Eline and its unusual penetration and impacts over the southern Africa. Weather Forecast 19:789-805

Reason CJC, Rouault M (2002) ENSO-like decadal patterns and South African rainfall. Geophys Res Lett 29. doi:10.1029/2002GL014663

Reynolds RW, Rayner NA, Smith TM, Stokes DC, Wang W (2002) An improved in situ and satellite SST analysis for climate. J Clim 15:1609–1625

Richard Y, Trzaska S, Roucou P, Rouault M (2000) Modification of the southern African rainfall variability/ENSO relationship since the late 1960s. Clim Dyn 16:883-895

Roeckner E, Arpe K, Bengtsson L, Christoph M, Claussen M, Dümenil L, Esch M, Giorgetta M, Schlese U, Schulzweida U (1996) The atmospheric general circulation model ECHAM-4: Model description and simulation of present-day climate. Tech. Rep. No. 218, Max-Planck-Institut für Meteorologie, Hamburg, Germany

Rouault M, Florenchie P, Fauchereau N, Reason CJC (2003) South East tropical Atlantic warm events and southern African rainfall. Geophys Res Lett 30. doi:10.1029/2002GL014840

Rouault M, Richard Y (2005) Spatial extent and intensity of droughts in southern Africa. Geophys Res Lett 32. doi:10.1029/2005GL022436

Saha S and Coauthors (2010) The NCEP climate forecast system reanalysis. Bull Amer

Meteor Soc 91:1015-1057

Schneider U, Becker A, Finger P, Meyer-Christoffer A, Xiese M, Rudolf B (2013) CGPP's new land surface precipitation climatology based on quality-controlled in situ data and its role in quantifying the global water cycle. Theor Appl Climatol. doi:10.1007/s00704-013-0860-x

Todd MC, Washington R (1999) Circulation anomalies associated with tropical-temperate troughs in southern Africa and the southwest Indian Ocean. Clim Dyn 15:937–951

Tozuka T, Luo JJ, Masson S, Behera SK, Yamagata T (2005) Annual ENSO simulated in a coupled ocean-atmosphere model. Dyn Atmos Ocean 39:41–60

Tozuka T, Abiodun BJ, Engelbrecht FA (2013) Impacts of convection schemes on simulating tropical-temperate troughs over southern Africa. Clim Dyn. doi:10.1007/s00382-013-1738-4

Tyson PD, Preston-Whyte RA (2004) The weather and climate of southern Africa. Oxford University Press, pp 232-244

Venegas SA, Mysak LA, Straub DN (1997) Atmosphere-ocean coupled variability in the South Atlantic. J Clim 10:2904–2920

Vigaud N, Richard Y, Rouault M, Fauchereau N (2009) Moisture transport between the South Atlantic Ocean and southern Africa: Relationships with summer rainfall and associated dynamics. Clim Dyn 32:113–123

Vigaud N, Pohl B, Crétat J (2012) Tropical-temperate interactions over southern Africa simulated by a regional climate model. Clim Dyn 39:2895-2916

Walker ND (1990) Links between South African summer rainfall and temperature variability of the Agulhas and Benguela Current systems. J Geophys Res 95:3297-3319

Wilks DS (1995) Statistical methods in the atmospheric sciences: An introduction. Academic Press, p 467.

Xie SP, Hu K, Hafner J, Tokinaga H, Du Y, Huang G, Sampe T (2009) Indian Ocean capacitor effects on Indo-Western Pacific climate during the summer following El Niño. J Clim 22:730-747

Yuan C, Tozuka T, Luo JJ, Yamagata T (2013) Predictability of subtropical dipole modes in a coupled ocean-atmosphere model. Clim Dyn. doi:10.1007/s00382-013-1704-1

Figure Captions

Figure 1: Mean precipitation (shading, in mm day^{-1}) and moisture flux at 850 hPa (vector, in kg m^{-1} s^{-1}) over southern Africa during DJF in (a) GPCP and NCEP/NCAR reanalysis 1, (b) GPCC and ERA-Interim, (c) ARC2 and CFSR, and (d) ensemble-mean forecasts initialized on October 1st for the period of 1982-2008. The white box in (a) denotes the area used to define the southern African precipitation index in this study.

Figure 2: Time series of the southern African precipitation indices in DJF. Years in the x-axis represent the three-month-mean period from December of that year till the following February. Black (blue) solid line represents the index derived from GPCP (ensemble-mean forecasts initialized on October 1st). Also shown are the box-and-whisker plots for the nine ensemble members at each year; the red boxes represent the interquartile ranges of the middle 56% ensemble members (five out of nine members). Green horizontal bars within the red boxes indicate precipitation anomalies of the median member, and red cross symbols show the maximum and minimum precipitation anomalies from the nine members.

Figure 3: Anomaly correlation coefficients (ACCs) of the deterministic forecasts initialized on October 1st for precipitation anomalies in DJF when verified against (a) GPCP, (b) GPCC and (c) ARC2 for the period of 1982 to 2008. White dashed contours denote ACCs of 0.32, significant at 95% confidence level by the one-tailed *t*-test.

Figure 4: Leave-one-out cross-validated (a) ROC and (b) ROL scores for the probabilistic forecasts of (blue) above- and (red) below-normal southern African precipitation in DJF. The probabilistic forecasts are initialized on October 1st and verified against

GPCP, GPCC and ARC2. The threshold value for above (below)-normal tercile is the lowest (highest) value in the highest (lowest) 33% of the historical records. The score of 0.7 is significant at 95% confidence level by the Mann-Whitney U-test.

Figure 5: Spatial distribution of the leave-one-out cross-validated ROC scores for the probabilistic forecasts of (a-c) above- and (d-f) below-normal precipitation. The forecasts are initialized on October 1st and verified against (a, d) GPCP, (b, e) GPCC and (c, f) ARC2. The threshold value for above (below)-normal tercile is the lowest (highest) value in the highest (lowest) 33% of the historical records. White dashed contours denote the score of 0.7, which is significant at 95% confidence level by the Mann-Whitney U-test.

Figure 6: As in Fig. 5, but for the leave-one-out cross-validated ROL scores.

Figure 7: Reliability diagrams and frequency histograms of the probabilistic forecasts initialized on October 1st for (blue) above- and (red) below-normal precipitation over southern Africa in DJF when verified against (a) GPCP, (b) GPCC and (c) ARC2. The solid lines denote the reliability curves, the filled vertical bars the frequencies of forecast probabilities, and the dotted lines the linear regression of the reliability curves weighted by the frequencies of forecast probabilities. The threshold value for above (below)-normal tercile is the lowest (highest) value in the highest (lowest) 33% of the historical records.

Figure 8: Composites of precipitation anomalies (mm day^{-1}) in DJF for (a-b) above- and (c-d) below-normal precipitation years that are successfully predicted by the model

initialized on October 1st. Here, (a, c) GPCP and (b, d) ensemble-mean forecasts are used. The stippling denotes anomalies significant at 90% confidence level.

Figure 9: Composites of geopotential height (shading, in m) and wind (vector, in m s^{-1}) anomalies at 850 hPa in DJF for (a, c, e, g) above- and (b, d, f, h) below-normal precipitation years that are successfully predicted by the model initialized on October 1st. Geopotential height anomalies significant at 90% confidence level are stippled and only wind anomalies significant at 90% confidence level are shown. Here, (a, b) NCEP/NCAR, (c, d) ERA-Interim, (e, f) CFSR and (g, h) ensemble-mean forecasts are used.

Figure 10: Composites of the specific humidity anomalies (kg kg^{-1}) in (a-d) above- and (e-h) below-normal precipitation years that are successfully predicted by the model initialized on October 1st. Here, (a, e) NCEP/NCAR, (b, f) ERA-Interim, (c, g) CFSR and (d, h) ensemble-mean forecasts are used. The stippling denotes anomalies significant at 90% confidence level.

Figure 11: As in Fig. 10, but for outgoing longwave radiation anomalies (W m^{-2}).

Figure 12: As in Fig. 8, but for SST anomalies (˚C) in (a, c) OISST and (b, d) ensemble-mean forecasts initialized on October 1st.

Figure 13: As in Fig. 9, but for the composites of (a, c, e, g) four La Niña and (b, d, f, h) four El Niño during the period of 1982-2008. Here, 1984/1985, 1988/1989, 1999/2000, and 2009/2010 (1982/1983, 1986/1987, 1991/1992 and 1997/1998) are defined as La Niña (El Niño) years following Ratnam et al. (2013a).

Figure 14: Observed and model correlation coefficients between precipitation anomalies and

(a, d) Niño-3, (b, e) South Atlantic subtropical dipole and (c, f) Indian Ocean subtropical dipole indices in DJF for the period of 1982-2008. The precipitation and SST data used are (a-c) OISST and GPCP and (d-f) ensemble-mean forecasts initialized on October 1st.

Figure 15: Eleven-year sliding correlation coefficients between (black line) the observed and predicted southern African summer precipitation indices in DJF, (blue line) the observed and predicted Benguela Niño indices in DJF, and (red line) the observed southern African precipitation and Niño-3 indices (multiplied by -1) in DJF. The year in the x-axis represents the central year of the eleven-year sliding window. The observed data used are GPCP and OISST and the forecasts are initialized on October 1st. The Benguela Niño index is defined as SST anomalies averaged from 10˚ to 20˚S and 8˚E to the coast following Florenchie et al. (2003).

Figure 16: ACCs of 3-month-mean precipitation anomalies in southern Africa for (a-d) October-December, (e-h) November-January, (i-l) December-February, (m-p) January-March and (q-t) February-April. The forecasts are at (a, e, i, m, q) 1-3, (b, f, j, n, r) 2-4, (c, g, k, o, s) 3-5 and (d, h, l, p, t) 4-6 months lead and the initialization dates are shown on the top of each panel. The GPCP is used for verification. White dashed contours denote ACCs of 0.32, significant at 95% confidence level by the one-tailed *t*-test.

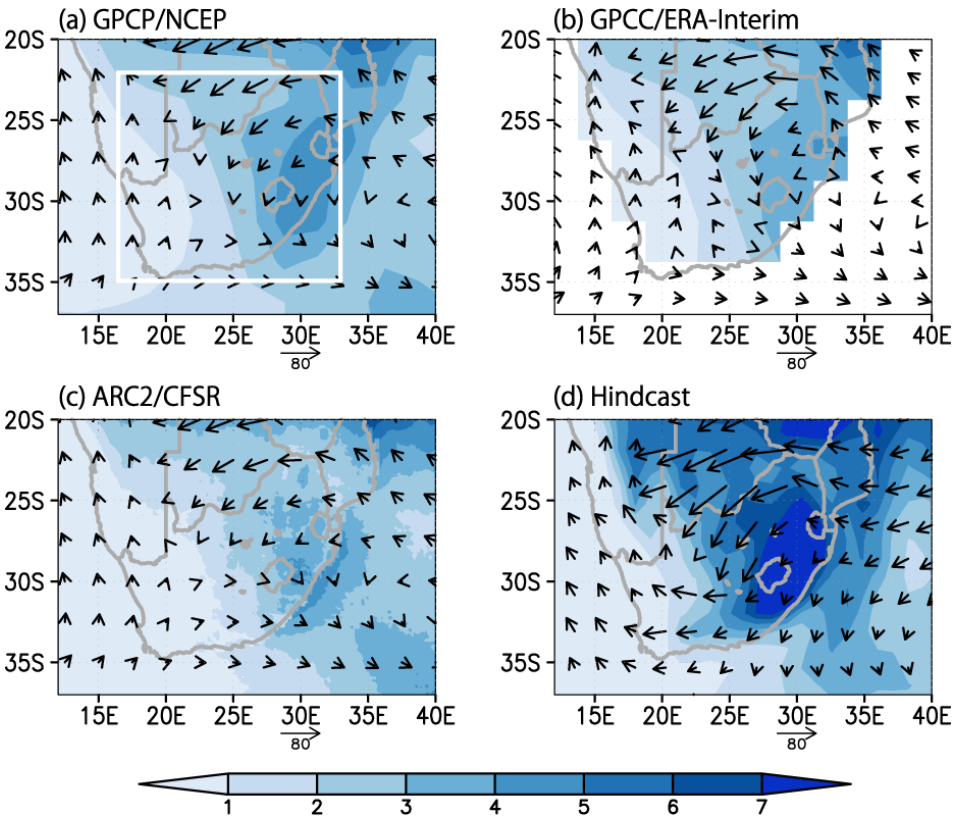

Figure 1: Mean precipitation (shading, in mm day^{-1}) and moisture flux at 850 hPa (vector, in kg m^{-1} s^{-1}) over southern Africa during DJF in (a) GPCP and NCEP/NCAR reanalysis 1, (b) GPCC and ERA-Interim, (c) ARC2 and CFSR, and (d) ensemble-mean forecasts initialized on October 1st for the period of 1982-2008. The white box in (a) denotes the area used to define the southern African precipitation index in this study.

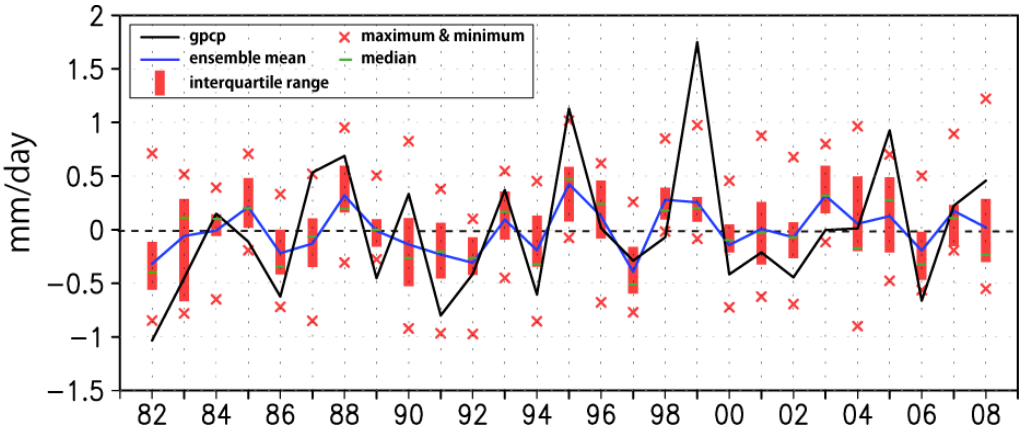

Figure 2: Time series of the southern African precipitation indices in DJF. Years in the x-axis represent the three-month-mean period from December of that year till the following February. Black (blue) solid line represents the index derived from GPCP (ensemble-mean forecasts initialized on October 1st). Also shown are the box-and-whisker plots for the nine ensemble members at each year; the red boxes represent the interquartile ranges of the middle 56% ensemble members (five out of nine members). Green horizontal bars within the red boxes indicate precipitation anomalies of the median member, and red cross symbols show the maximum and minimum precipitation anomalies from the nine members.

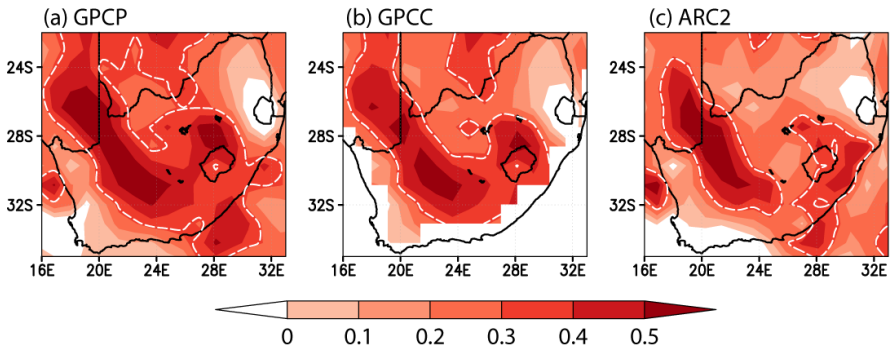

Figure 3: Anomaly correlation coefficients (ACCs) of the deterministic forecasts initialized on October 1st for precipitation anomalies in DJF when verified against (a) GPCP, (b) GPCC and (c) ARC2 for the period of 1982 to 2008. White dashed contours denote ACCs of 0.32, significant at 95% confidence level by the one-tailed *t*-test.

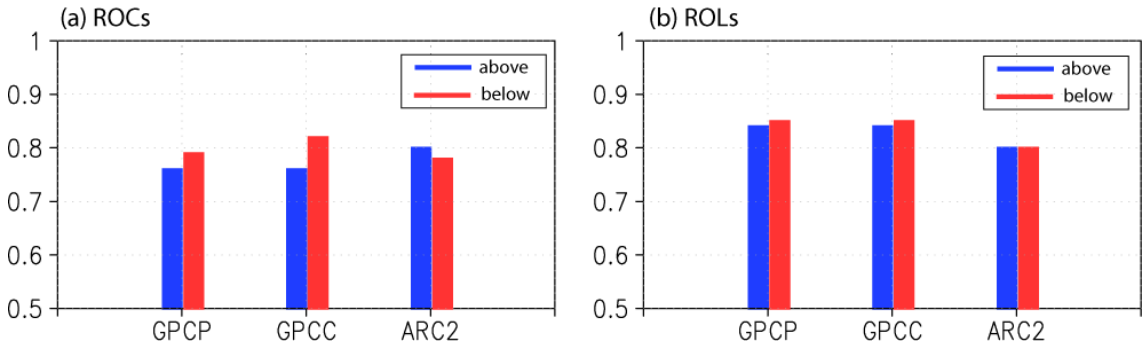

Figure 4: Leave-one-out cross-validated (a) ROC and (b) ROL scores for the probabilistic forecasts of (blue) above- and (red) below-normal southern African precipitation in DJF. The probabilistic forecasts are initialized on October 1st and verified against GPCP, GPCC and ARC2. The threshold value for above (below)-normal tercile is the lowest (highest) value in the highest (lowest) 33% values of the historical records. The score of 0.7 is significant at 95% confidence level by the Mann-Whitney U-test.

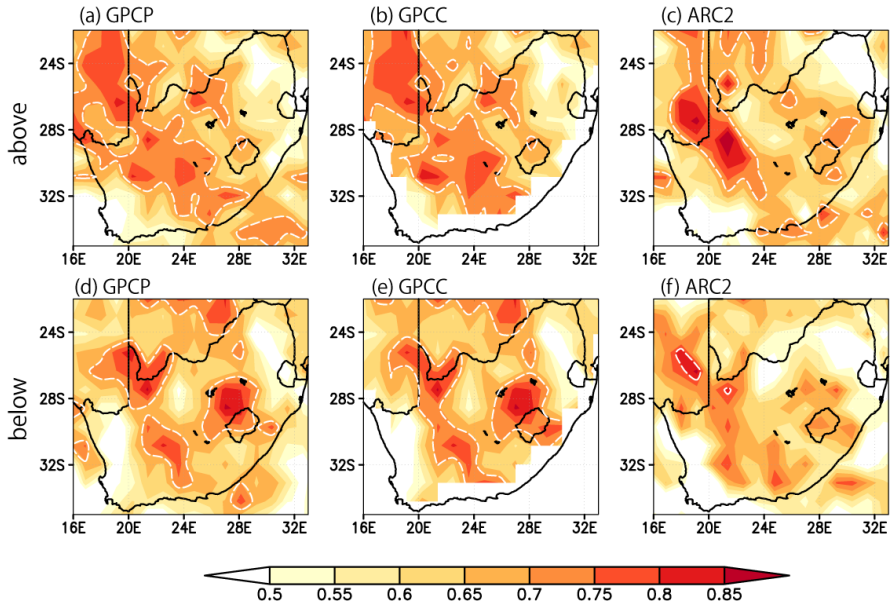

Figure 5: Spatial distribution of the leave-one-out cross-validated ROC scores for the probabilistic forecasts of (a-c) above- and (d-f) below-normal precipitation. The forecasts are initialized on October 1st and verified against (a, d) GPCP, (b, e) GPCC and (c, f) ARC2. The threshold value for above (below)-normal tercile is the lowest (highest) value in the highest (lowest) 33% values of the historical records. White dashed contours denote the score of 0.7, which is significant at 95% confidence level by the Mann-Whitney U-test.

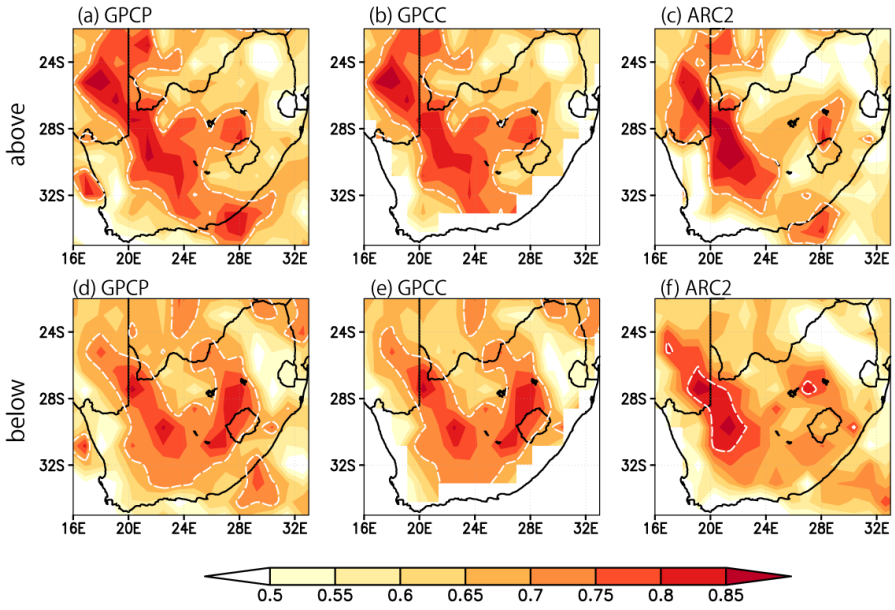

Figure 6: As in Fig. 5, but for the leave-one-out cross-validated ROL scores.

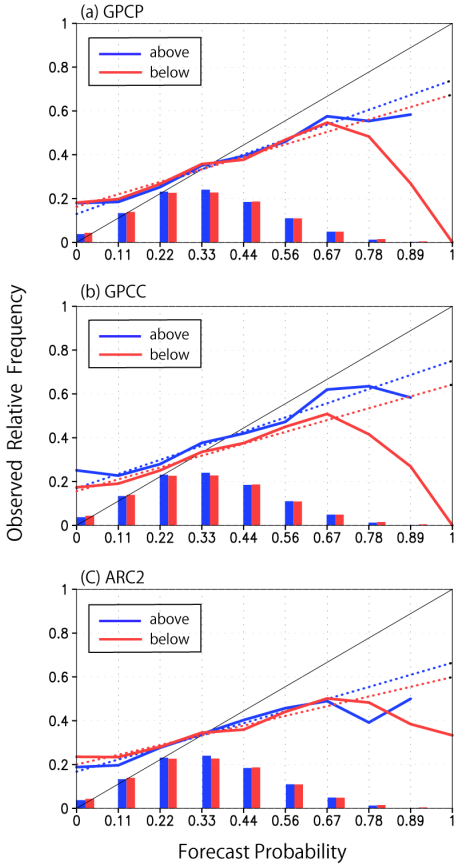

Figure 7: Reliability diagrams and frequency histograms of the probabilistic forecasts initialized on October 1st for (blue) above- and (red) below-normal precipitation over southern Africa in DJF when verified against (a) GPCP, (b) GPCC and (c) ARC2. The solid lines denote the reliability curves, the filled vertical bars the frequencies of forecast probabilities, and the dotted lines the linear regression of the reliability curves weighted by the frequencies of forecast probabilities. The threshold value for above (below)-normal tercile is the lowest (highest) value in the highest (lowest) 33% of the historical records.

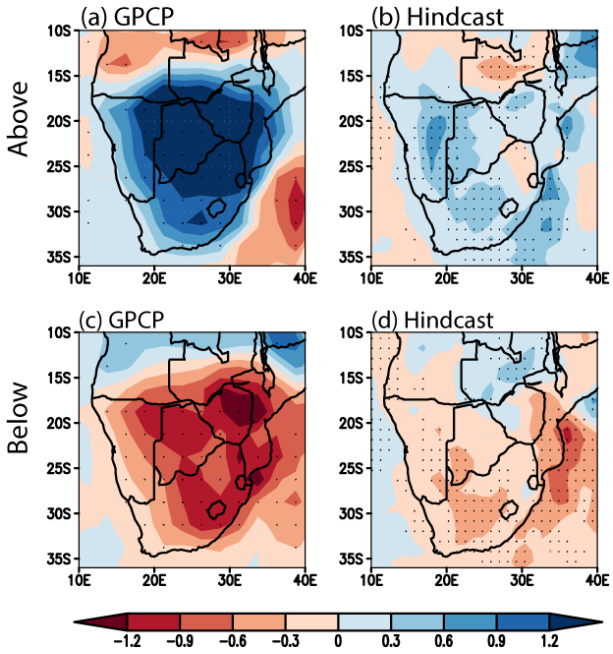

igure 8: Composites of precipitation anomalies (mm day^{-1}) in DJF for (a-b) above- and (c-d) elow-normal precipitation years that are successfully predicted by the model initialized on ctober 1st. Here, (a, c) GPCP and (b, d) ensemble-mean forecasts are used. The stippling enotes anomalies significant at 90% confidence level.

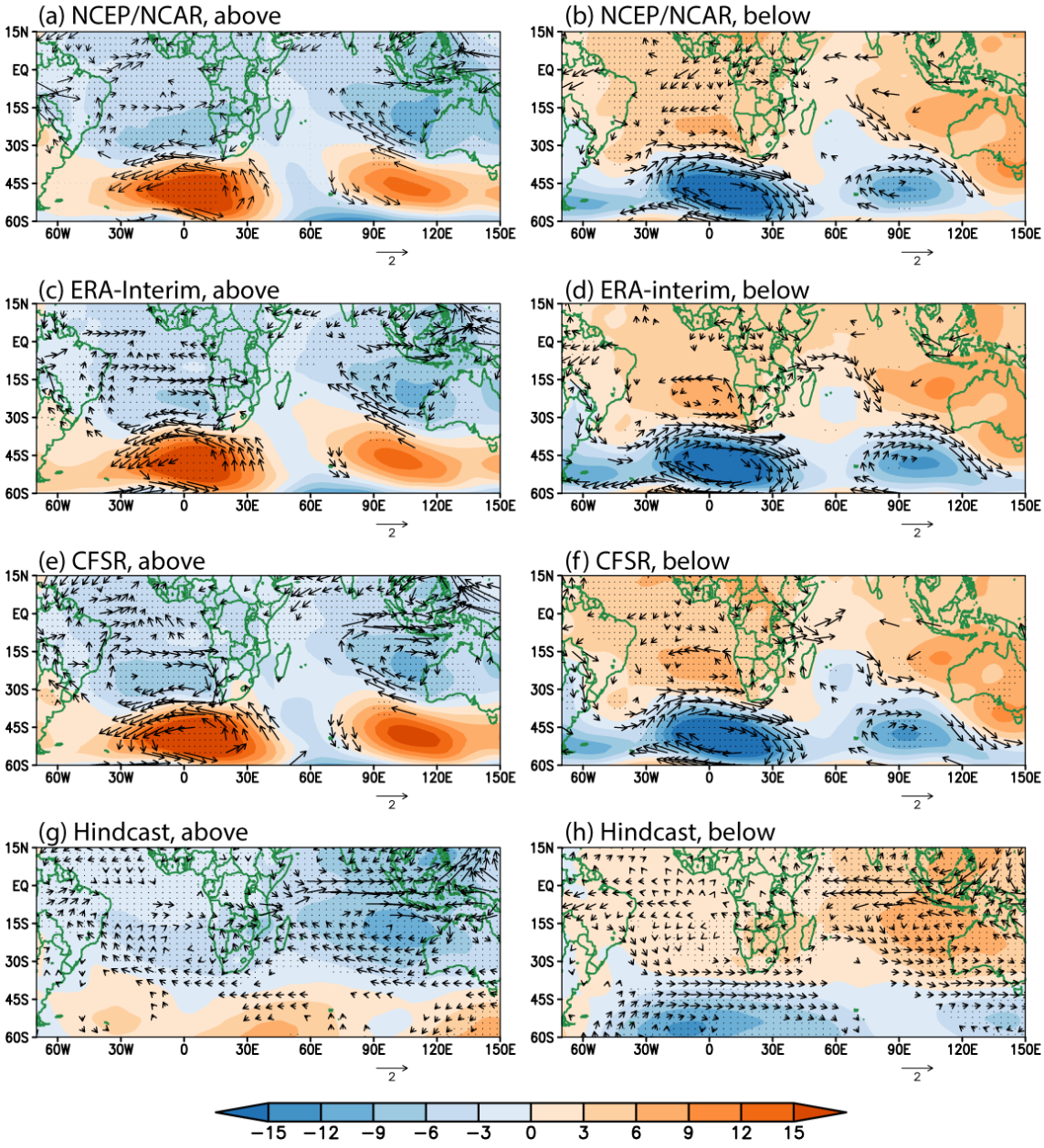

Figure 9: Composites of geopotential height (shading, in m) and wind (vector, in m s^{-1}) anomalies at 850 hPa in DJF for (a, c, e, g) above- and (b, d, f, h) below-normal precipitation years that are successfully predicted by the model initialized on October 1st. Geopotential height anomalies significant at 90% confidence level are stippled and only wind anomalies significant at 90% confidence level are shown. Here, (a, b) NCEP/NCAR, (c, d) ERA-Interim, (e, f) CFSR and (g, h) ensemble-mean forecasts are used.

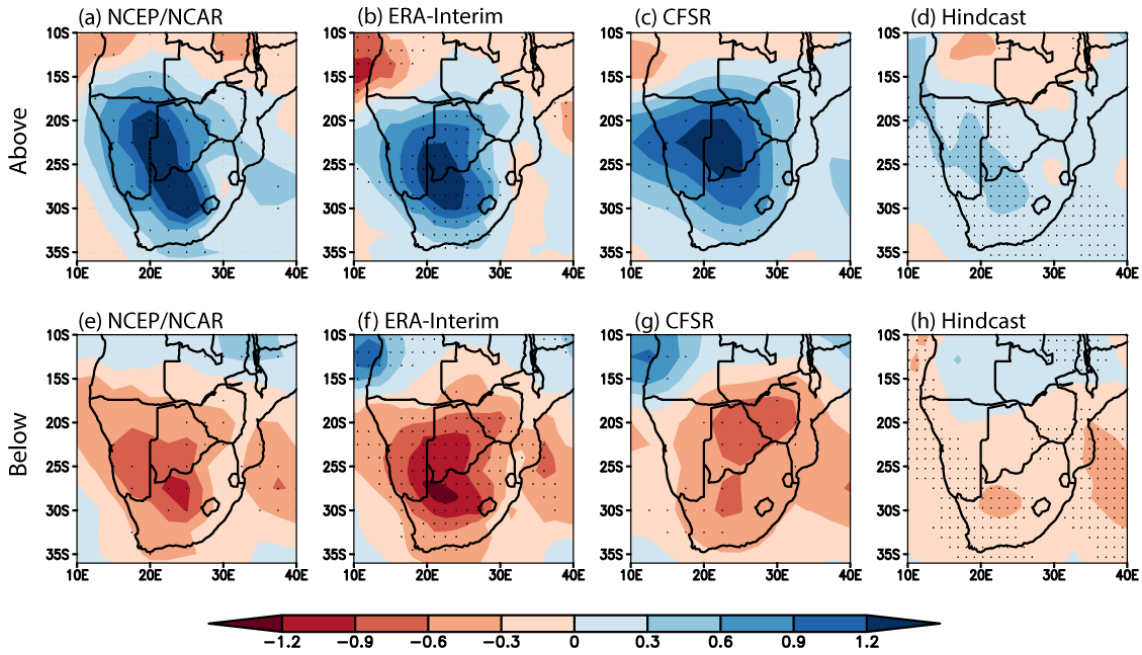

Figure 10: Composites of the specific humidity anomalies (kg kg^{-1}) in (a-d) above- and (e-h) below-normal precipitation years that are successfully predicted by the model initialized on October 1st. Here, (a, e) NCEP/NCAR, (b, f) ERA-Interim, (c, g) CFSR and (d, h) ensemble-mean forecasts are used. The stippling denotes anomalies significant at 90% confidence level.

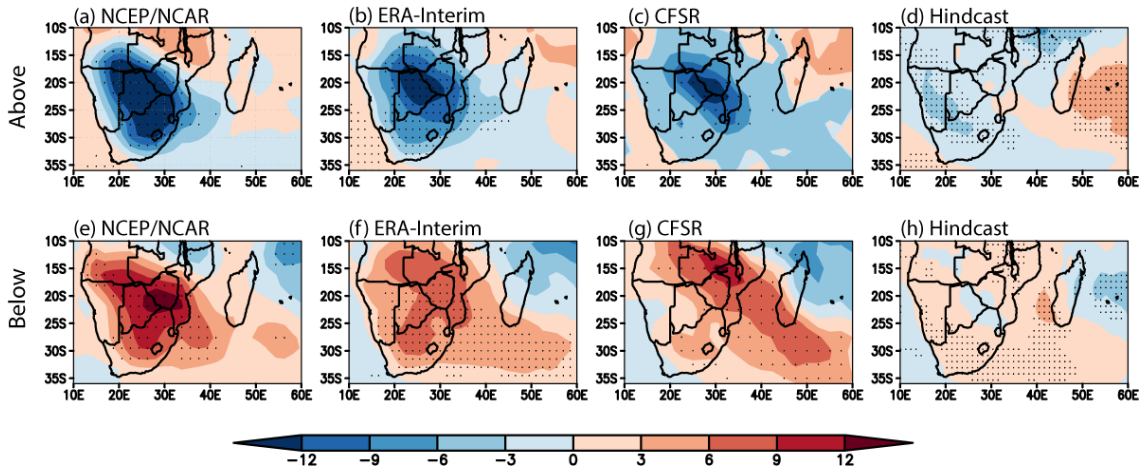

Figure 11: As in Fig. 10, but for outgoing longwave radiation anomalies (W m^{-2}).

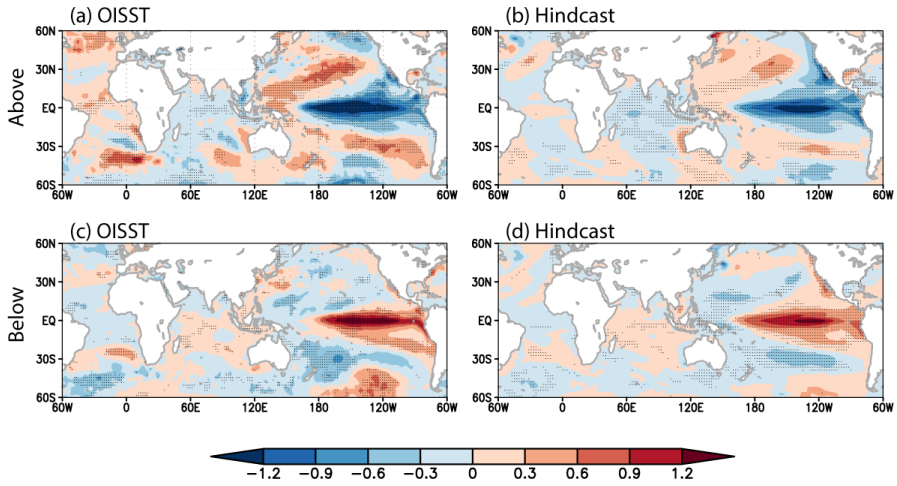

Figure 12: As in Fig. 8, but for SST anomalies (˚C) in (a, c) OISST and (b, d) ensemble-mean forecasts initialized on October 1st.

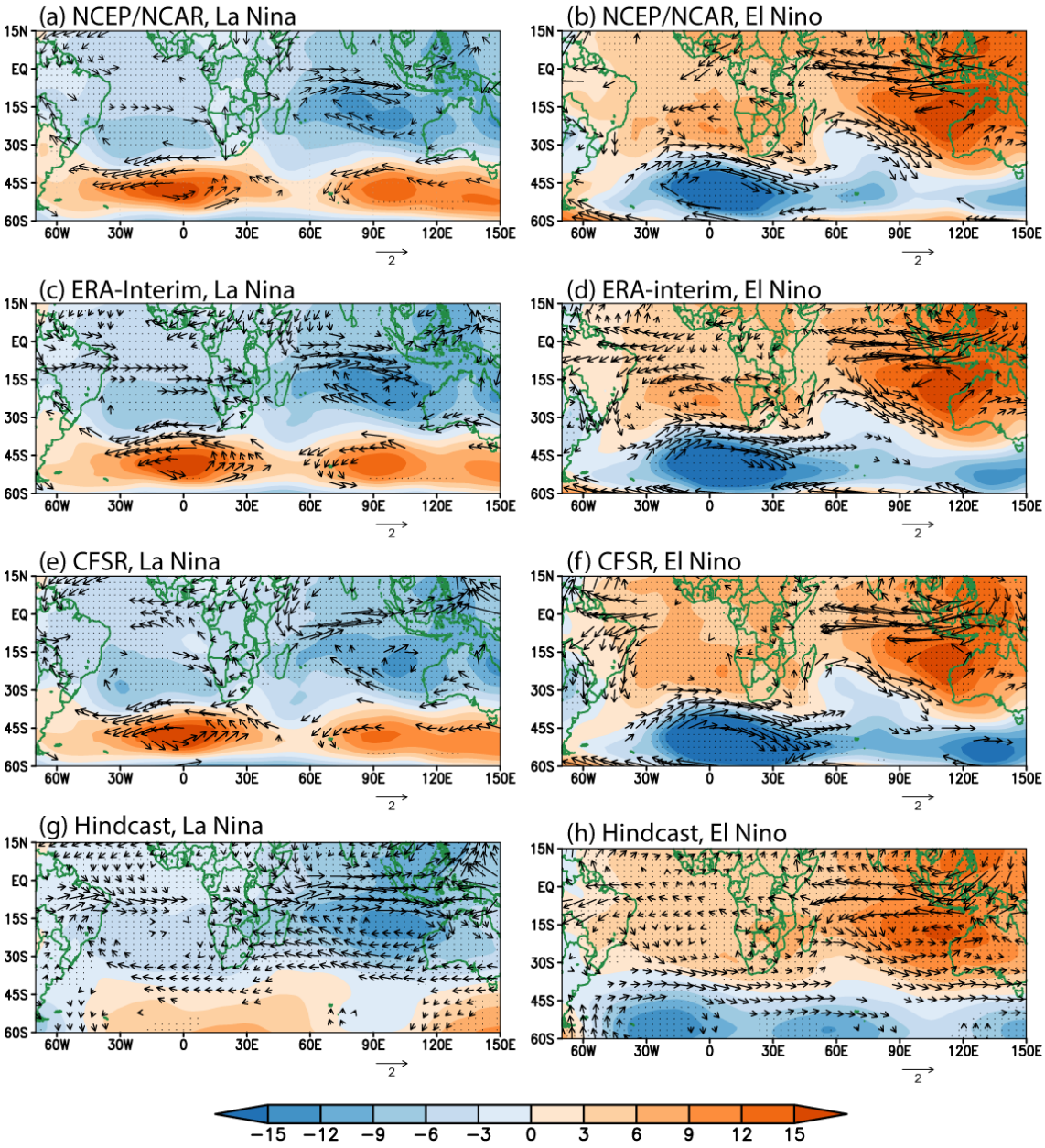

Figure 13: As in Fig. 9, but for the composites of (a, c, e, g) four La Niña and (b, d, f, h) four El Niño during the period of 1982-2008. Here, 1984/1985, 1988/1989, 1999/2000, and 2009/2010 (1982/1983, 1986/1987, 1991/1992 and 1997/1998) are defined as La Niña (El Niño) years following Ratnam et al. (2013a).

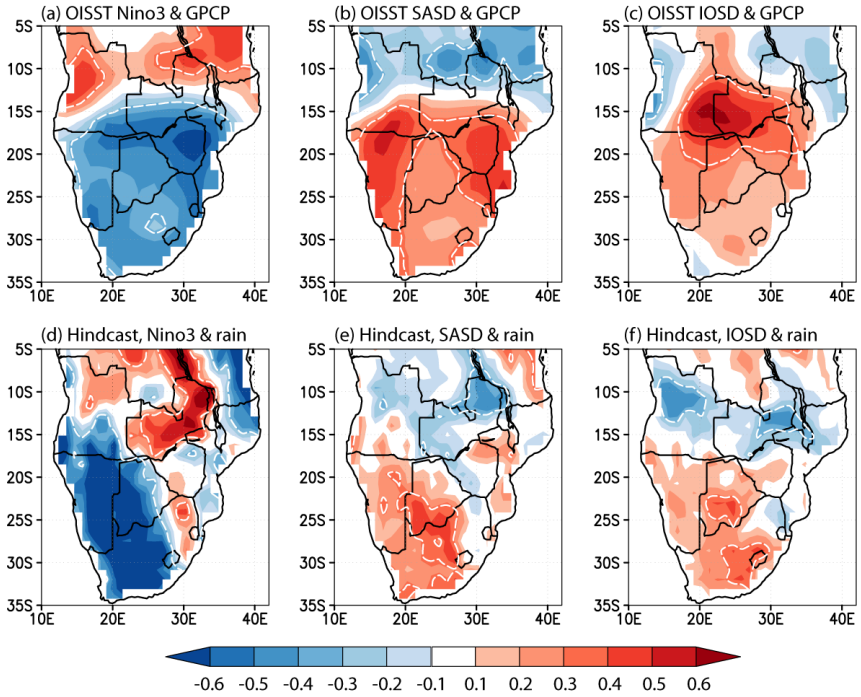

Figure 14: Observed and model correlation coefficients between precipitation anomalies and (a, d) Niño-3, (b, e) South Atlantic subtropical dipole and (c, f) Indian Ocean subtropical dipole indices in DJF for the period of 1982-2008. The precipitation and SST data used are (a-c) OISST and GPCP and (d-f) ensemble-mean forecasts initialized on October 1st.

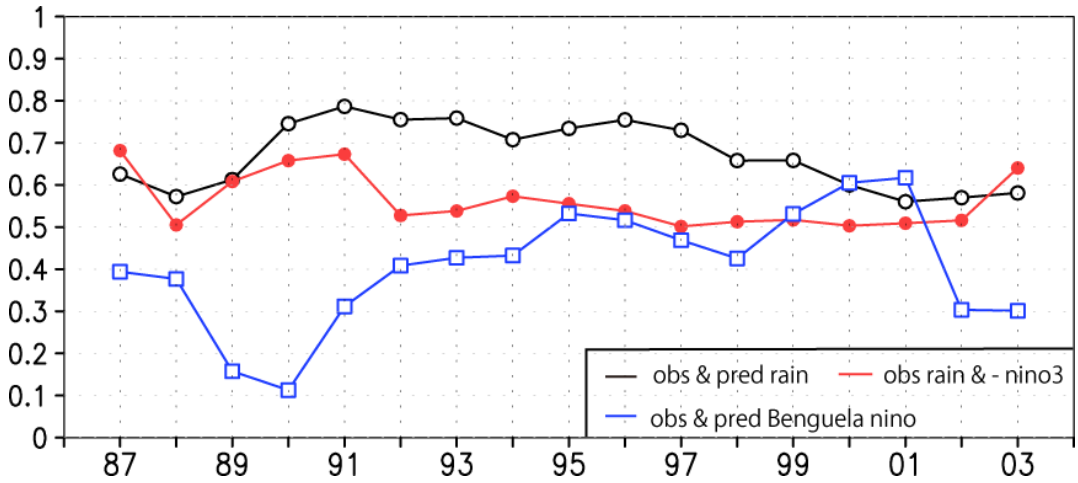

Figure 15: Eleven-year sliding correlation coefficients between (black line) the observed and predicted southern African summer precipitation indices in DJF, (blue line) the observed and predicted Benguela Niño indices in DJF, and (red line) the observed southern African precipitation and Niño-3 indices (multiplied by -1) in DJF. The year in the x-axis represents the central year of the eleven-year sliding window. The observed data used are GPCP and OISST and the forecasts are initialized on October 1st. The Benguela Niño index is defined as SST anomalies averaged from 10˚ to 20˚S and 8˚E to the coast following Florenchie et al. (2003).

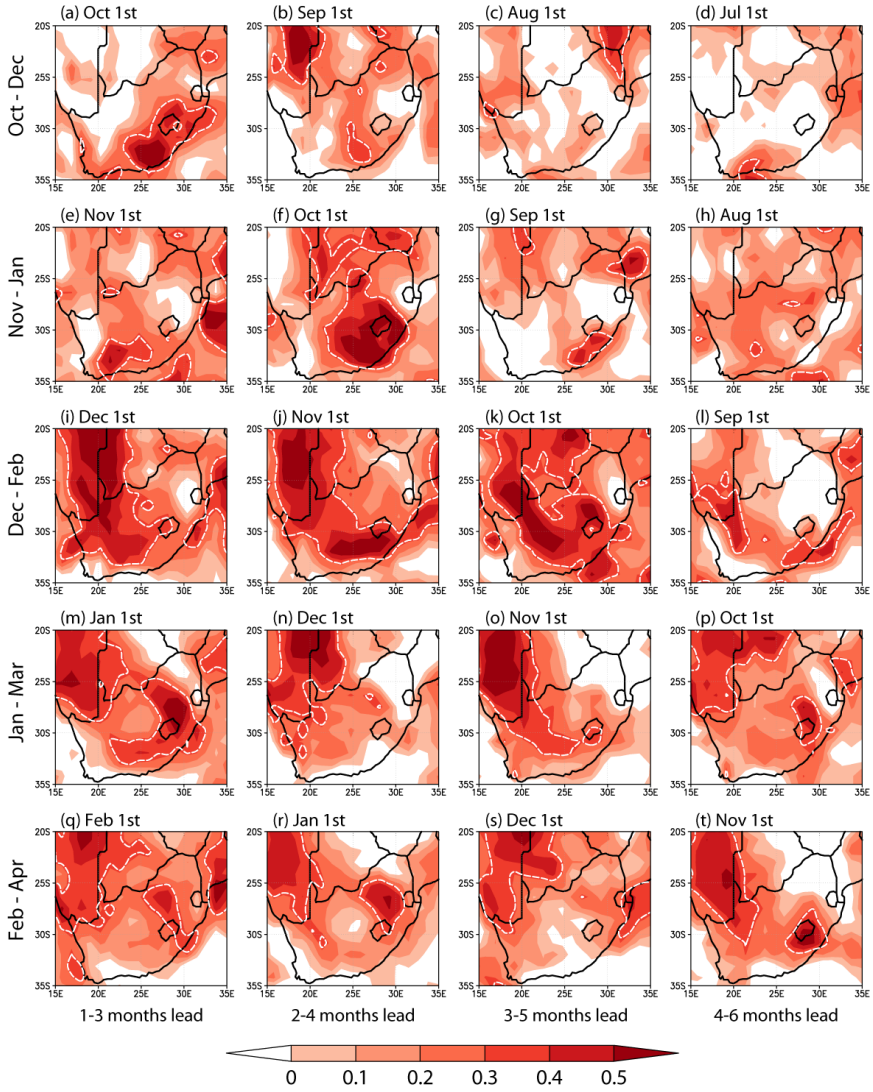

Figure 16: ACCs of 3-month-mean precipitation anomalies in southern Africa for (a-d) October-December, (e-h) November-January, (i-l) December-February, (m-p) January-March and (q-t) February-April. The forecasts are at (a, e, i, m, q) 1-3, (b, f, j, n, r) 2-4, (c, g, k, o, s) 3-5 and (d, h, l, p, t) 4-6 months lead and the initialization dates are shown on the top of each panel. The GPCP is used for verification. White dashed contours denote ACCs of 0.32, significant at 95% confidence level by the one-tailed *t*-test.